

Catalog of Selected Color Figures

From the Book *Cosmology* by Daniel Baumann

The figures in this file can be downloaded individually from the following websites:

www.cambridge.org/baumann
github.com/ddbaumann/cosmo-book

Please feel free to use these figures for any non-commercial purposes. A reference to the book would be greatly appreciated.

In the future, I may create color versions of additional figures from the book. I may also produce alternative versions of the figures presented here. Please let me know if you have suggestions for improving these figures.

Daniel Baumann
Amsterdam and Taipei, 2022

Hubble Diagram

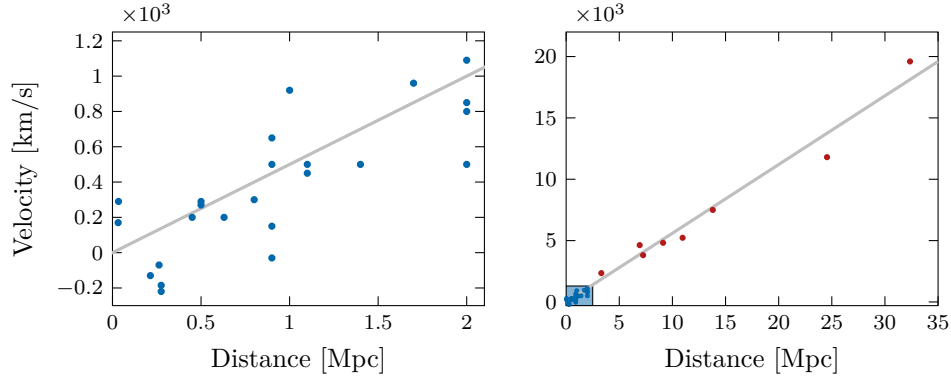


Fig. 2.4 Historical measurements of the velocity–distance relationship in an expanding universe. The left plot shows Hubble’s original data from 1929, including an optimistic linear fit to Hubble’s law [1]. The right plot includes additional data from 1931 collected together with Humason [2]. Both measurements contain systematic errors and overestimate Hubble’s constant significantly, $H_0 \approx 500 \text{ km s}^{-1} \text{ Mpc}^{-1}$.

Galaxy Rotation Curve

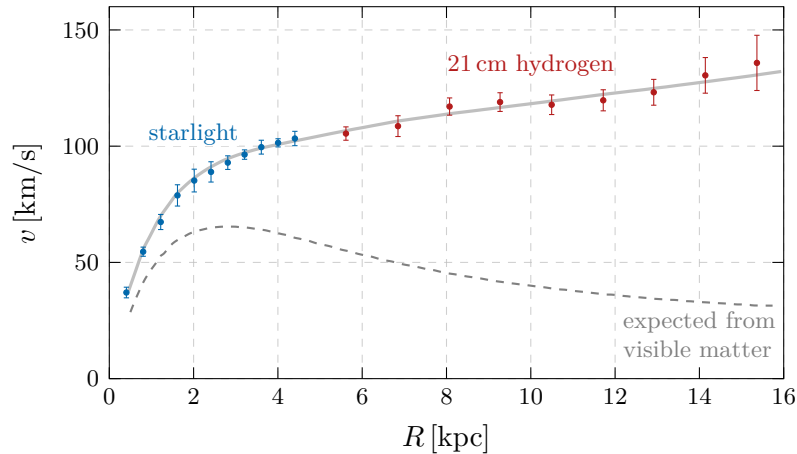


Fig. 2.9 Rotation curve of M33 (figure adapted from [3]). The dashed line is the expected rotation curve accounting only for the visible matter in the stellar disc. The data clearly shows the need for an additional dark matter component.

Evolution of Energy Densities

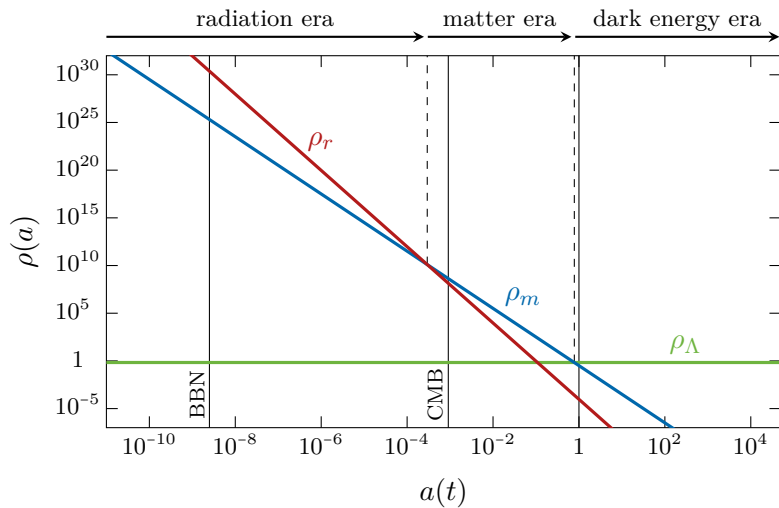


Fig. 2.10 Evolution of the energy densities in the universe. We see that there is often one dominant component: first radiation, then matter and finally dark energy. Sometimes two components are relevant during the transitions between the different eras.

CMB Power Spectrum

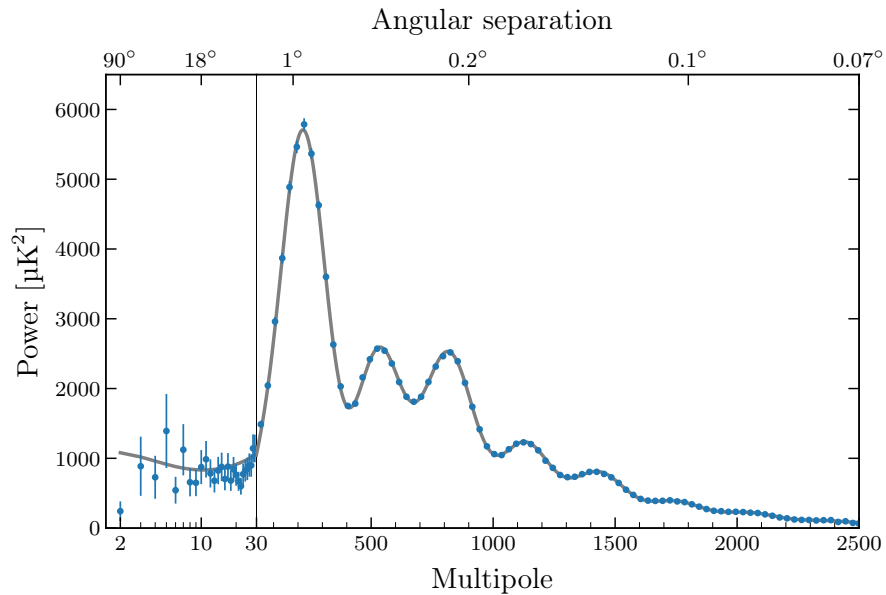


Fig. 2.14 The power spectrum of CMB temperature anisotropies as measured by the Planck satellite [4]. The position of the first peak depends on the spatial curvature of the universe. The height of the first peak is a measure of the matter density and the relative heights of the other peaks determine the baryon density.

Modern Hubble Diagram

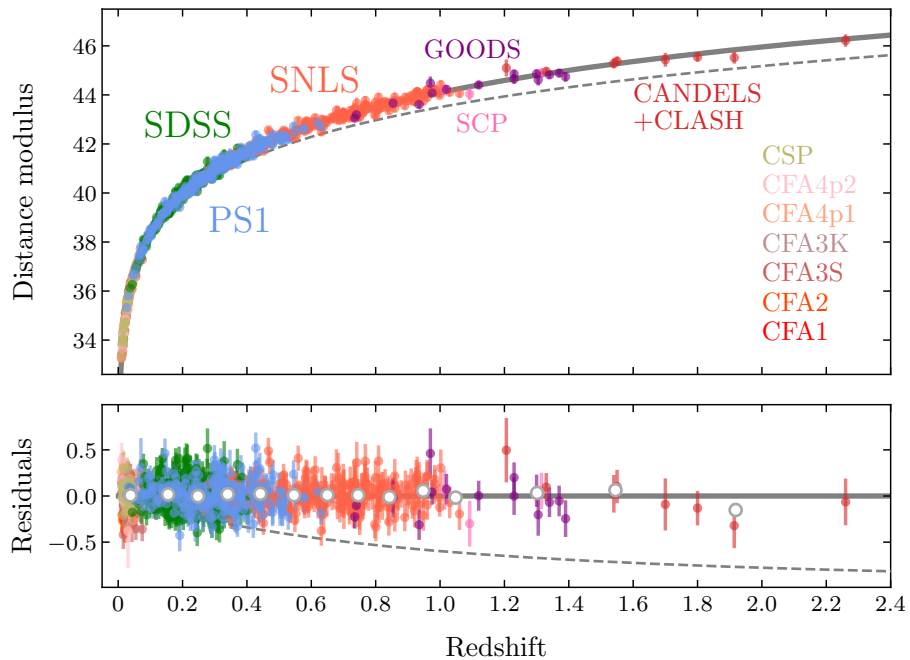


Fig. 2.15

Distance-redshift relationship of 1048 supernovae from the Pantheon sample [5]. The solid line is the best-fit Λ CDM model (with $\Omega_m = 0.32$ and $\Omega_\Lambda = 0.68$), while the dashed line is for a flat matter-only universe (with $\Omega_m = 1.0$). The supernovae clearly appear fainter (or more distant) than predicted in a matter-only universe. The lower panel shows the residuals relative to the Λ CDM best-fit model, with binned data given by the white points.

CMB Last Scattering

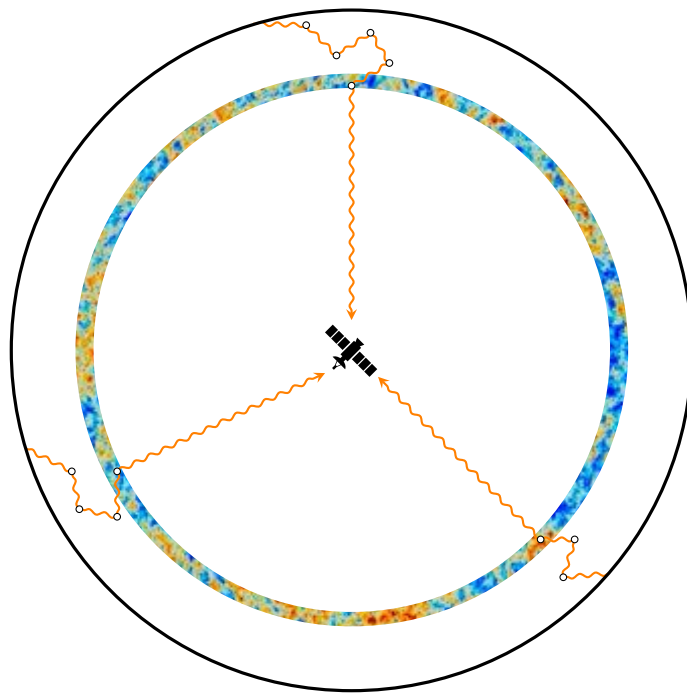


Fig. 3.7 Cartoon of the last-scattering of CMB photons after recombination. Today we observe the CMB photons from the spherical surface of last-scattering.

CMB Blackbody Spectrum

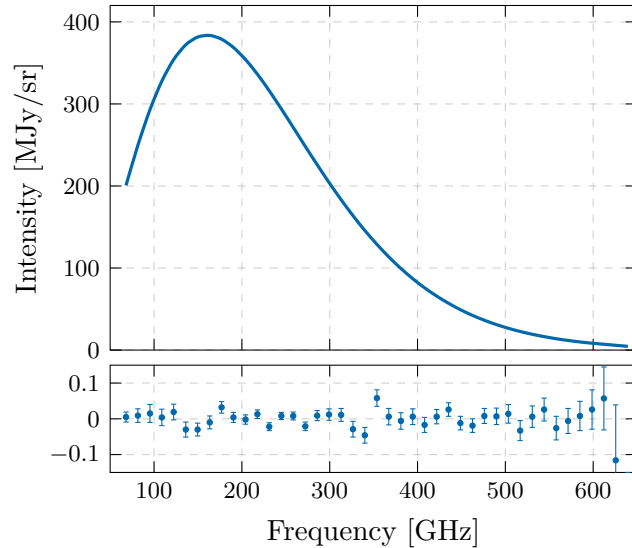


Fig. 3.8 Measurement of the CMB blackbody spectrum by the COBE satellite [6]. The error bars are too small to be seen in the top panel. In the bottom panel, we therefore also show the residuals relative to a blackbody spectrum with temperature $T_0 = 2.725$ K. Notice the change in scale between the two panels.

BBN: Predictions

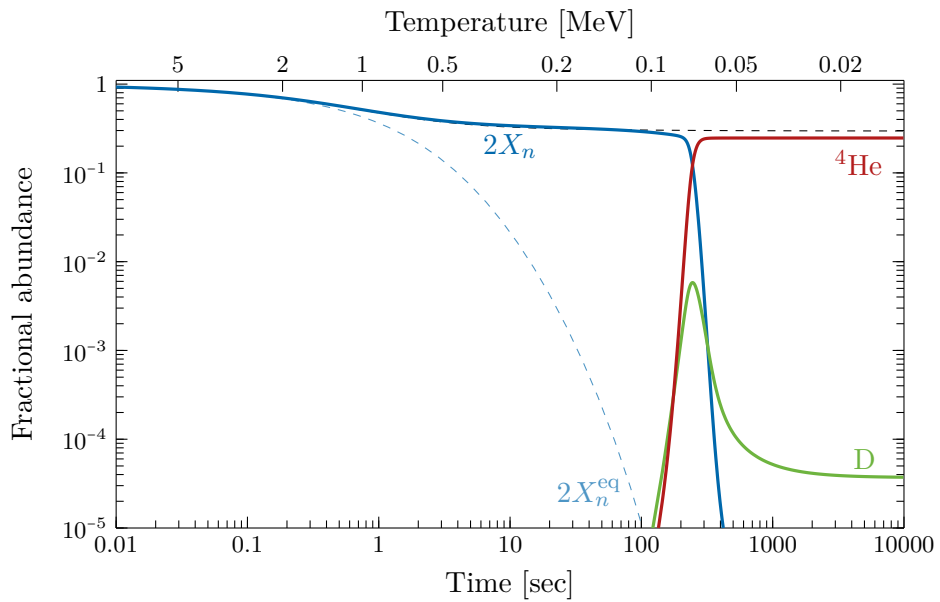


Fig. 3.13 Numerical result for the production of helium and deuterium in the early universe [7]. At early times, neutrons and protons are in equilibrium and their abundances are roughly equal. Around 1 MeV, the weak interactions become inefficient and the neutrons freeze out. Due to its low binding energy, it takes a while until neutrons and protons combine into deuterium. Once the fusion of deuterium has started, the subsequent production of helium is very rapid.

BBN: Observational Constraints

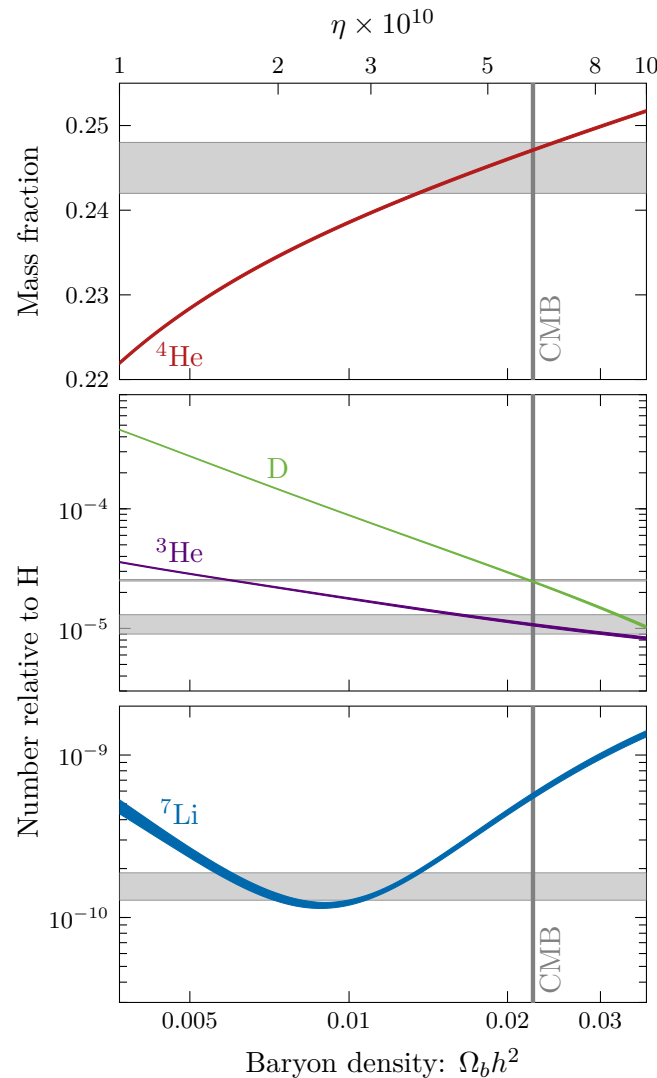


Fig. 3.14 Theoretical predictions for the light element abundances and observational constraints (gray bands) [7]. The line widths on the theory curves account for uncertainties in the neutron lifetime and the nuclear cross sections.

Recombination: Three-Level Atom

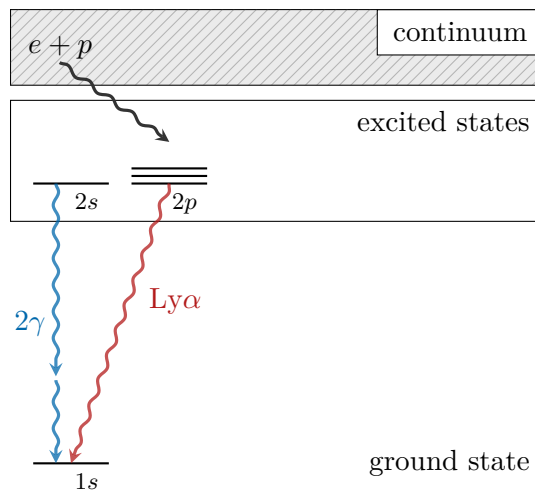


Fig. 3.15 Illustration of the Peebles model of recombination. Recombination directly to the ground state $1s$ is very inefficient. Instead, recombination proceeds first by capture of the electron to one of the excited states, which quickly cascade to the first excited states $2s$ and $2p$. These excited states then decay to the ground state at a much slower rate.

Matter Power Spectrum

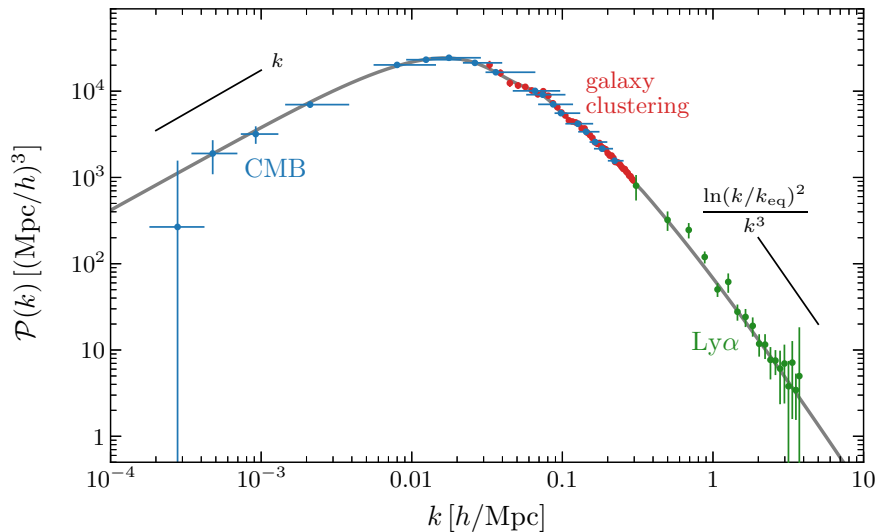


Fig. 5.2

Measurements of the linear matter power spectrum (figure adapted from [8]). The “galaxy clustering” constraints are from the luminous red galaxy sample of the Sloan Digital Sky Survey (SDSS). The “CMB” constraints are derived from the Planck measurements of the CMB temperature anisotropies. “Ly α ” refers to the Lyman-alpha forest. To avoid clutter, the plot doesn’t include constraints from CMB polarization, CMB lensing and galaxy shear. These can be found in [8].

Photon–Baryon Fluid and Decoupling

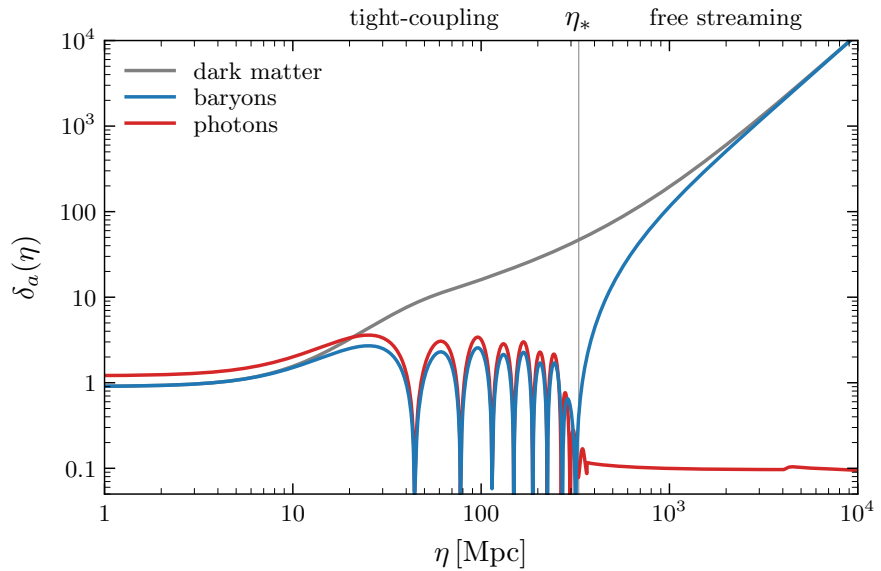


Fig. 6.8 Evolution of the density contrasts of dark matter (gray), baryons (blue) and photons (red) for $k = 0.25 h \text{ Mpc}^{-1}$. Note that around the time of decoupling the fluid approximation breaks down and the evolution is *not* captured by the equations described in this chapter. Instead, this figure was produced by solving the Boltzmann equations for the distribution functions of each species numerically.

Acoustic Peaks

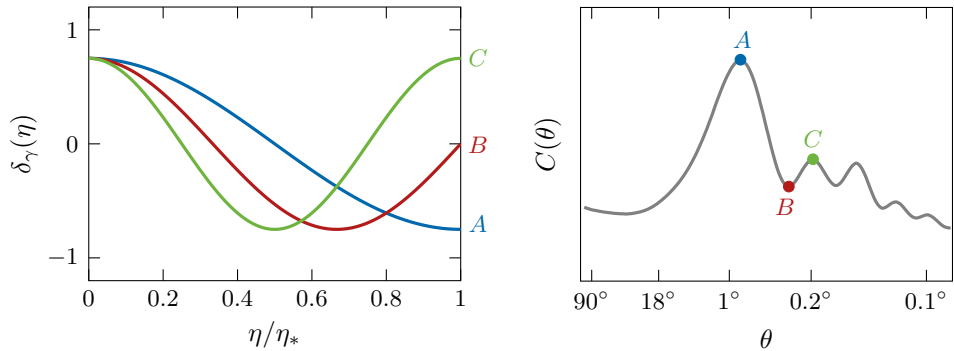


Fig. 6.10 Cartoon illustrating the origin of the peaks in the CMB power spectrum. *Left:* Fluctuations of different wavelengths are captured at different moments in their evolution and therefore have different amplitudes at decoupling. *Right:* Since the square of the amplitude determines the power on a given length scale, waves that are captured at an extremum (*A* or *C*) produce the peaks in the CMB spectrum, while waves that are captured with zero amplitude (*B*) produce the troughs.

Baryon Acoustic Oscillations

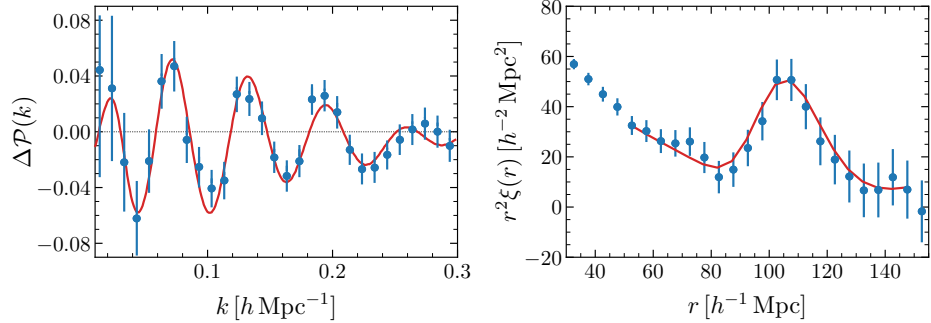


Fig. 6.12 Measurement of the BAO signal in Fourier space (*left*) and in real space (*right*). To accentuate the oscillatory feature, the left plot show the deviation $\Delta\mathcal{P}(k)$ from the smooth spectrum. (Figure adapted from [9].)

CMB Anisotropy Map

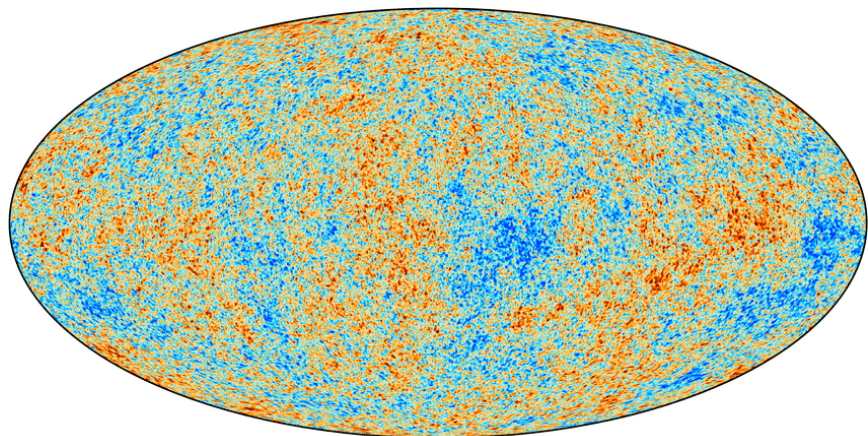


Fig. 7.1

Temperature fluctuations in the cosmic microwave background as measured by the Planck satellite [10].

CMB Power Spectrum

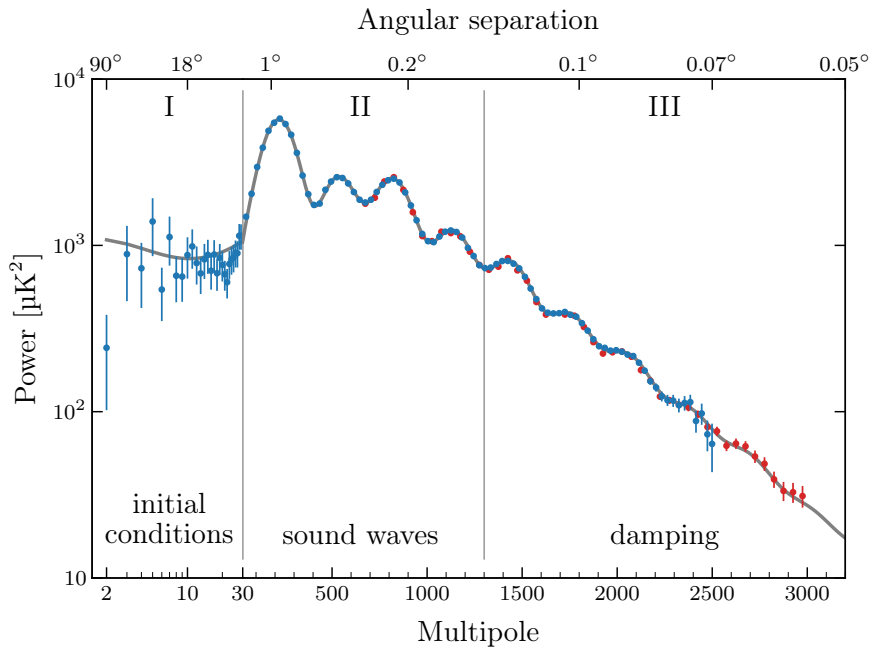


Fig. 7.2 Power spectrum of the CMB anisotropies measured by the Planck satellite (blue) [10] and the South Pole Telescope (red) [11]. For low multipoles (large angular scales), the spectrum is determined by the primordial initial conditions alone. For intermediate multipoles, the imprint of sound waves in the photon-baryon fluid is seen, while for large multipoles (small angular scales) damping becomes important. (To avoid clutter, I have not added relevant data from the Atacama Cosmology Telescope.)

Transfer Function of The Photon Density

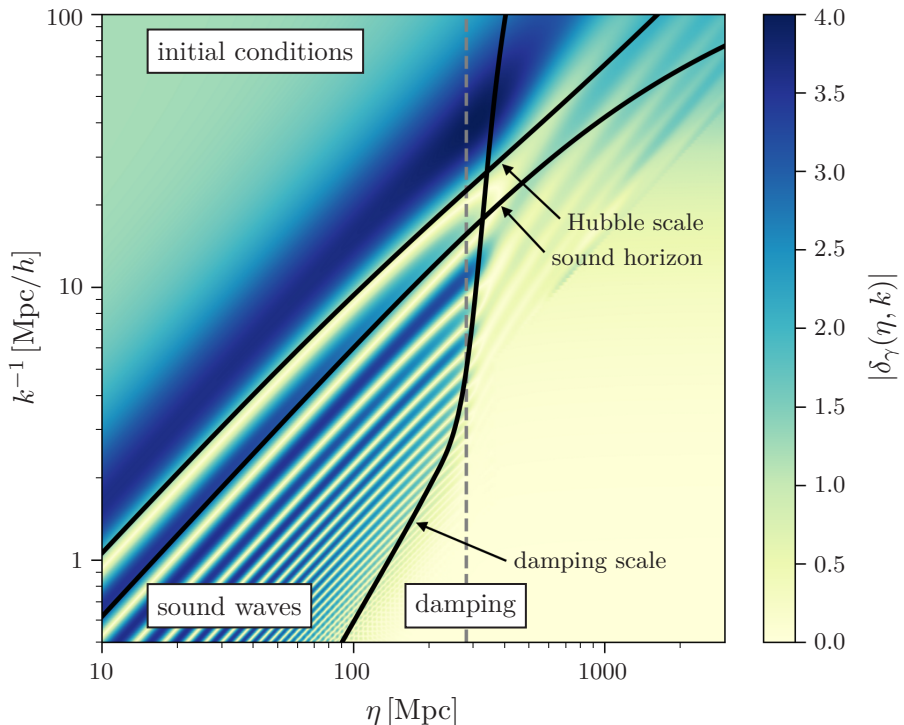


Fig. 7.10 Transfer function of the photon density contrast as a function of k and η , computed with CLASS [12]. Illustrated are also the evolution of the Hubble scale, the sound horizon and the damping scale, and the moment of recombination (dashed line). We see that sound waves propagate below the sound horizon and are suppressed below the damping scale.

CMB Spectra with Changing Parameters

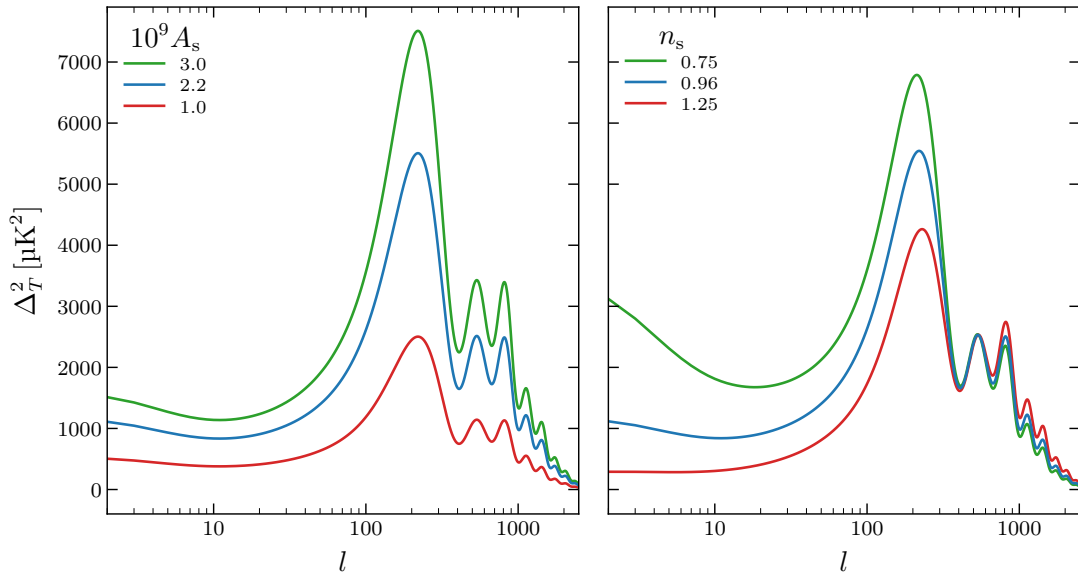


Fig. 7.19 Variation of the CMB power spectrum with changes of the amplitude A_s (*left*) and the tilt n_s (*right*) of the primordial power spectrum.

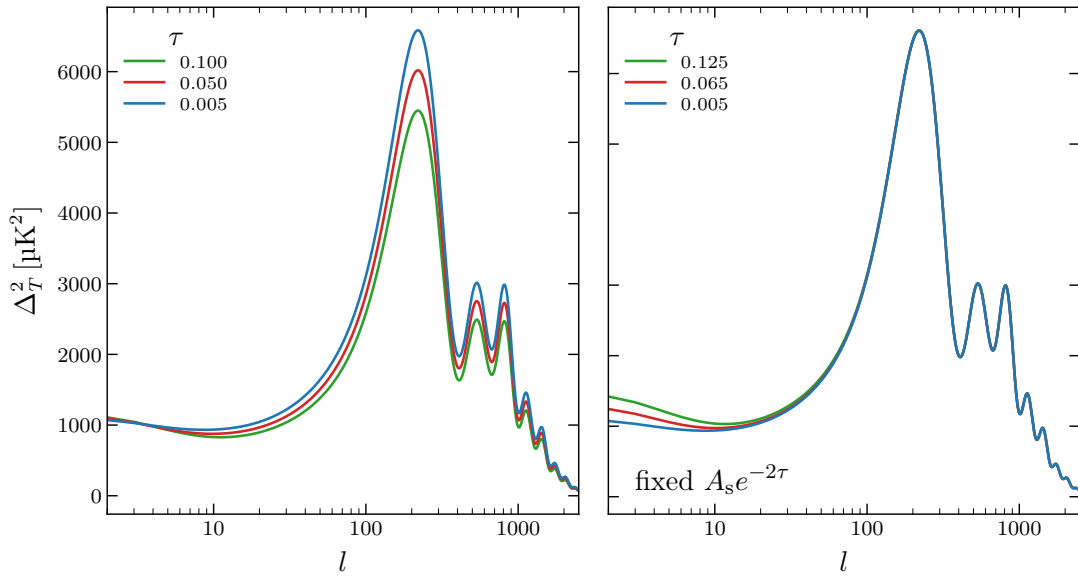


Fig. 7.20 Effect of reionization on the CMB power spectrum. In the right panel, the amplitude A_s has been adjusted to keep the combination $A_s e^{-2\tau}$ fixed.

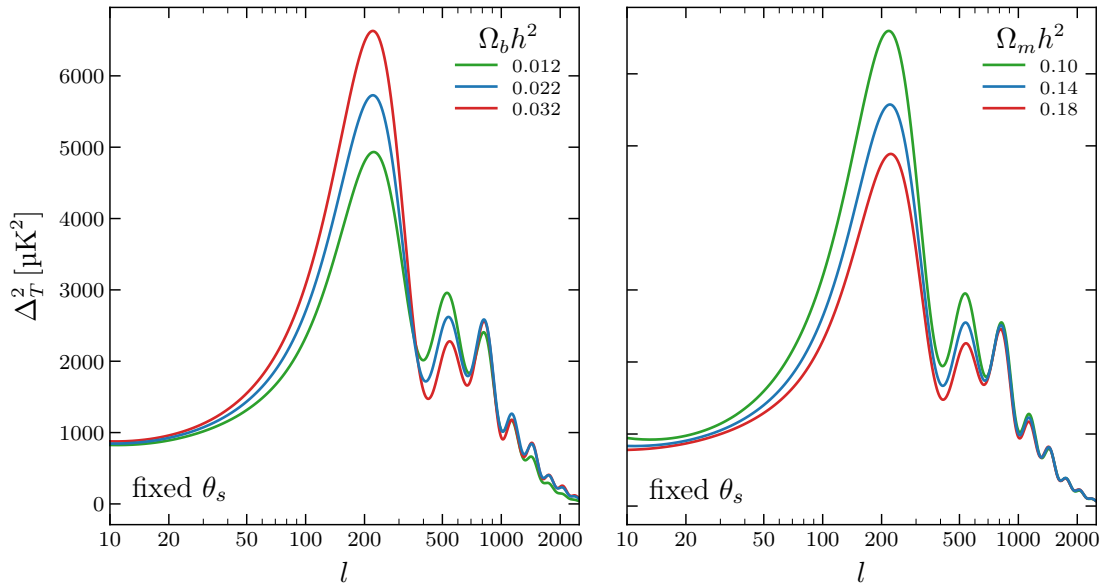


Fig. 7.21 Effects of varying the baryon density $\Omega_b h^2$ (*left*) and the matter density $\Omega_m h^2$ (*right*) at fixed angular scale of the sound horizon θ_s .

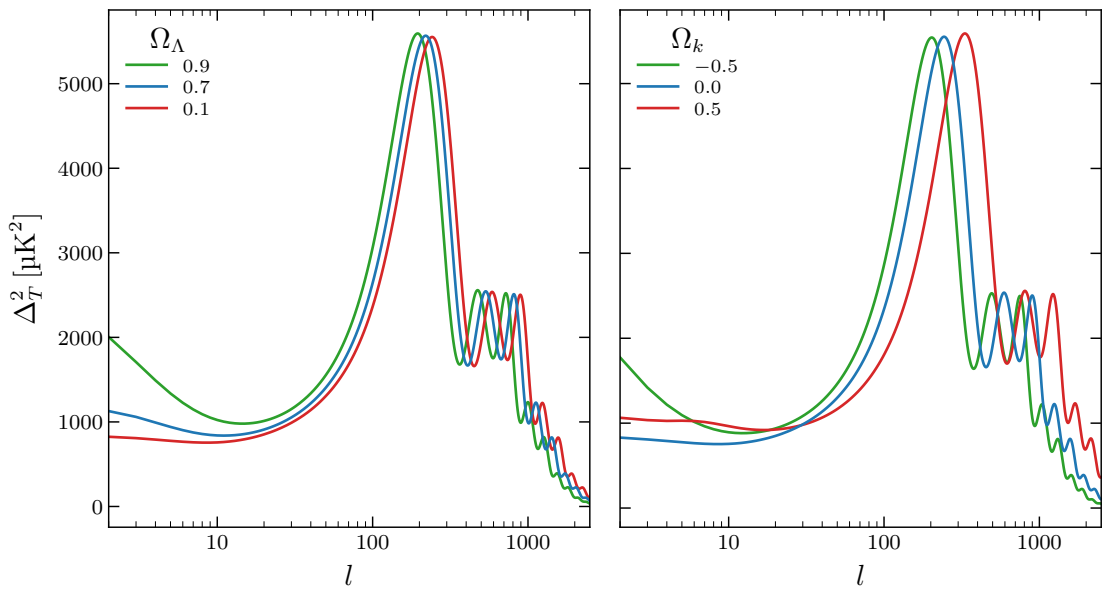


Fig. 7.22 Variation of the CMB power spectrum with dark energy density (*left*) and spatial curvature (*right*), keeping $\Omega_b h^2$ and $\Omega_m h^2$ fixed.

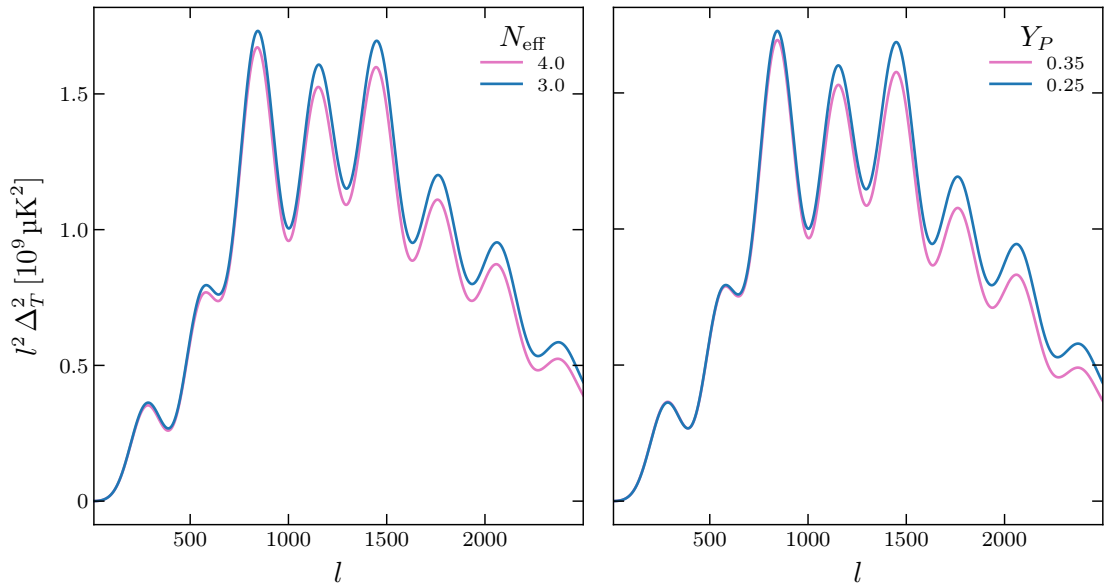


Fig. 7.23 Variation of the CMB temperature power spectrum as a function of N_{eff} (*left*) and Y_P (*right*) for fixed angular size of the sound horizon θ_s . The spectra have been multiplied by a factor of l^2 to emphasize the effects at large l .

Polarization from Thomson Scattering

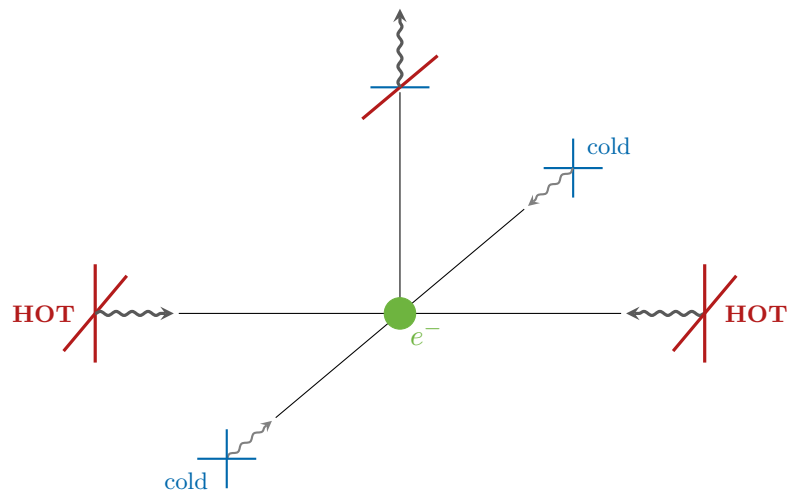


Fig. 7.26 A net polarization is generated if the incident radiation has a quadrupolar anisotropy. The polarization direction of the outgoing radiation is aligned with the hot regions.

E- and B-modes from a Plane Wave

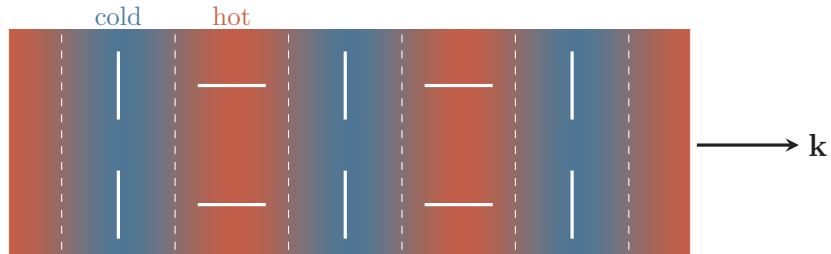


Fig. 7.27 Illustration of E-mode polarization created by a plane wave density perturbation. The sketched polarization pattern is for radiation scattering out of the plane of the paper. We see that the polarization directions are parallel or perpendicular to the wavevector \mathbf{k} .

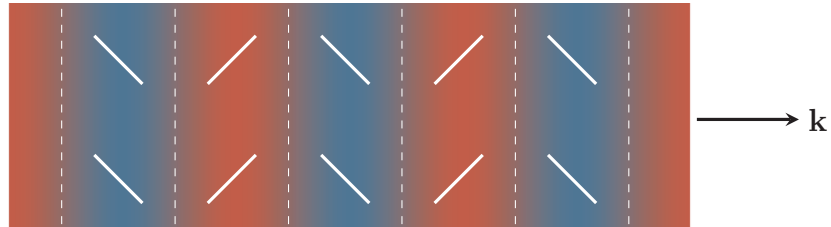


Fig. 7.28 Illustration of B-mode polarization created by a plane wave. The polarization directions are rotated by 45° relative to the E-mode pattern shown in Fig. 7.27. The azimuthal symmetry of scalar density fluctuations (i.e. rotational symmetry around \mathbf{k}) forbids such a polarization pattern.

Polarization Power Spectra

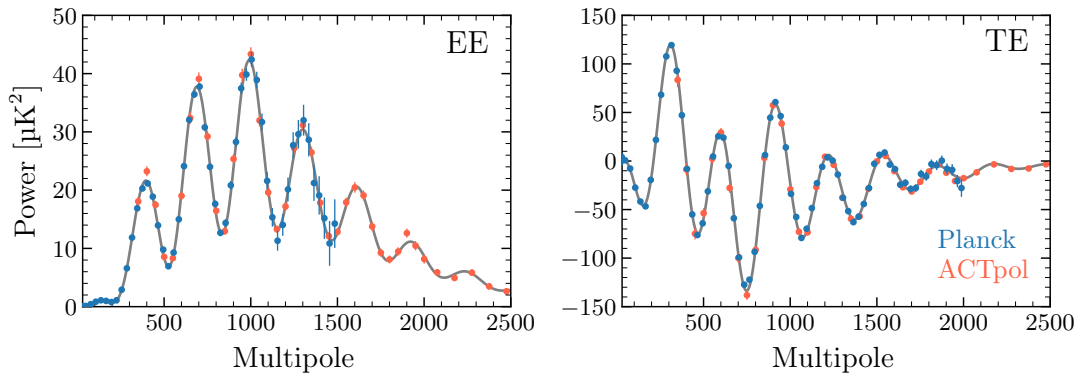


Fig. 7.30 E-mode power spectrum (*left*) and its cross correlation with the temperature fluctuations (*right*) measured by the Planck satellite and the Atacama Cosmology Telescope. The curves are not fits to the data, but instead are predictions given the parameters inferred from the fit to the temperature power spectrum. (To avoid clutter, I have not added relevant data from the South Pole Telescope.)

E- and B-modes from a Plane Wave

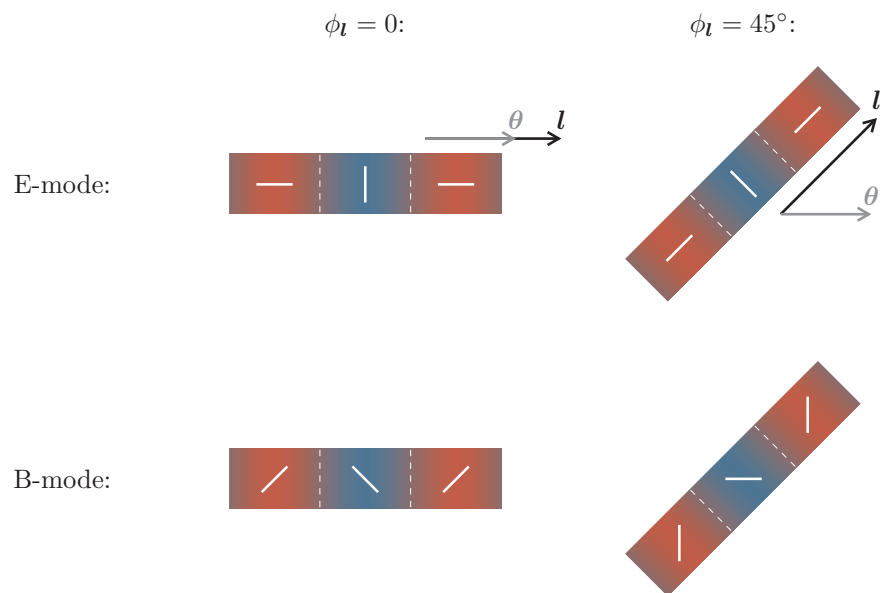


Fig. 7.31 Polarization patterns corresponding to a pure E-mode (*top*) and a pure B-mode (*bottom*) for two different orientations of the plane wave. We see that for the E-mode the polarization directions are either parallel or perpendicular to the wavevector, while for the B-mode they are tilted by 45° .

E- and B-modes from a Radial Wave

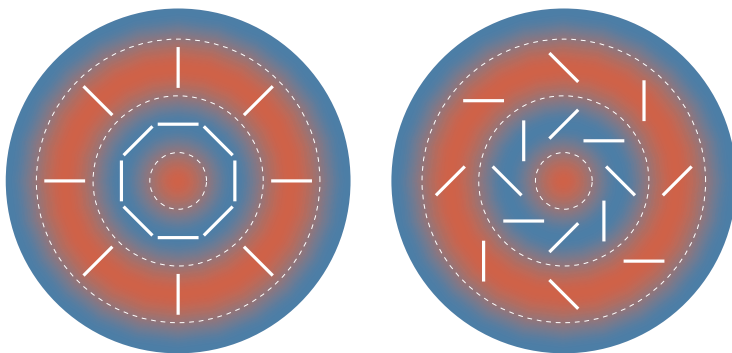


Fig. 7.32 E- and B-mode patterns created by a radial wave in the xy -plane for radiation in the z -direction (out of the page). Note that when reflected about a line going through the center, the E-mode pattern remains unchanged, while the B-mode pattern changes. (Figure adapted from [13].)

Polarization from a Gravitational Wave

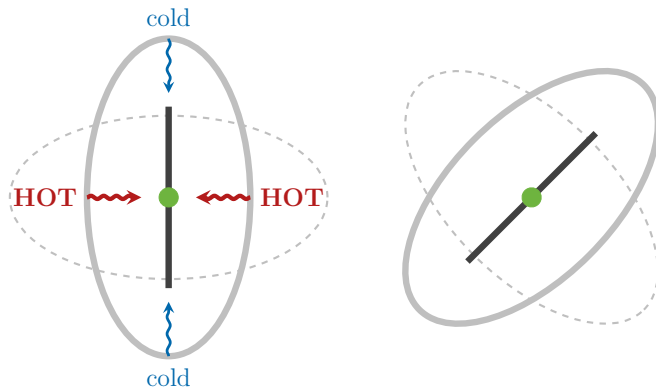


Fig. 7.35 Cartoon illustrating that the anisotropic stretching and compressing of space by a gravitational wave creates a temperature quadrupole and hence leads to CMB polarization. The two polarizations of the gravitational wave produce polarization of the CMB photons with a relative angle of 45° . This is why gravitational waves produce both E and B-modes, while density perturbations create only E-modes.

B-mode Power Spectrum

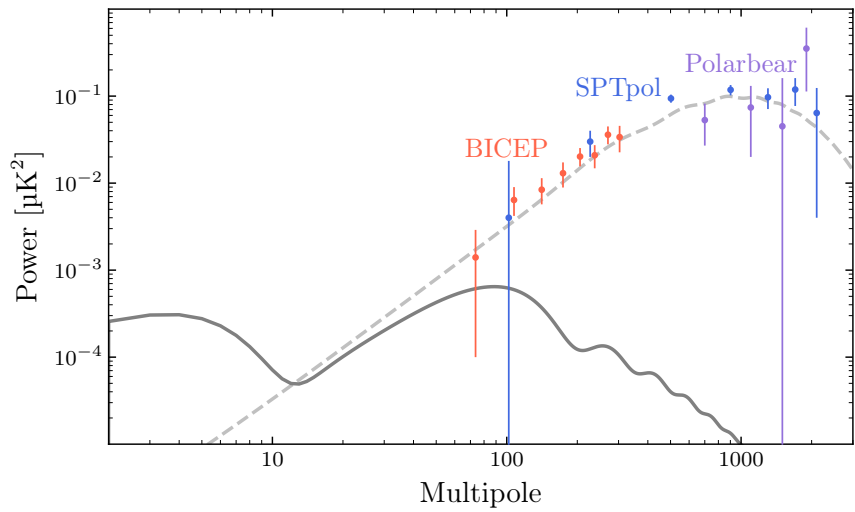


Fig. 7.36 Current measurements of the B-mode spectrum. The measurements have detected the lensing-induced B-modes (dashed line) but are not yet sensitive enough to reveal the primordial B-mode signal (solid line). Shown is the maximal allowed primordial B-mode signal corresponding to a tensor-to-scalar ratio of $r = 0.035$.

CMB Spectra

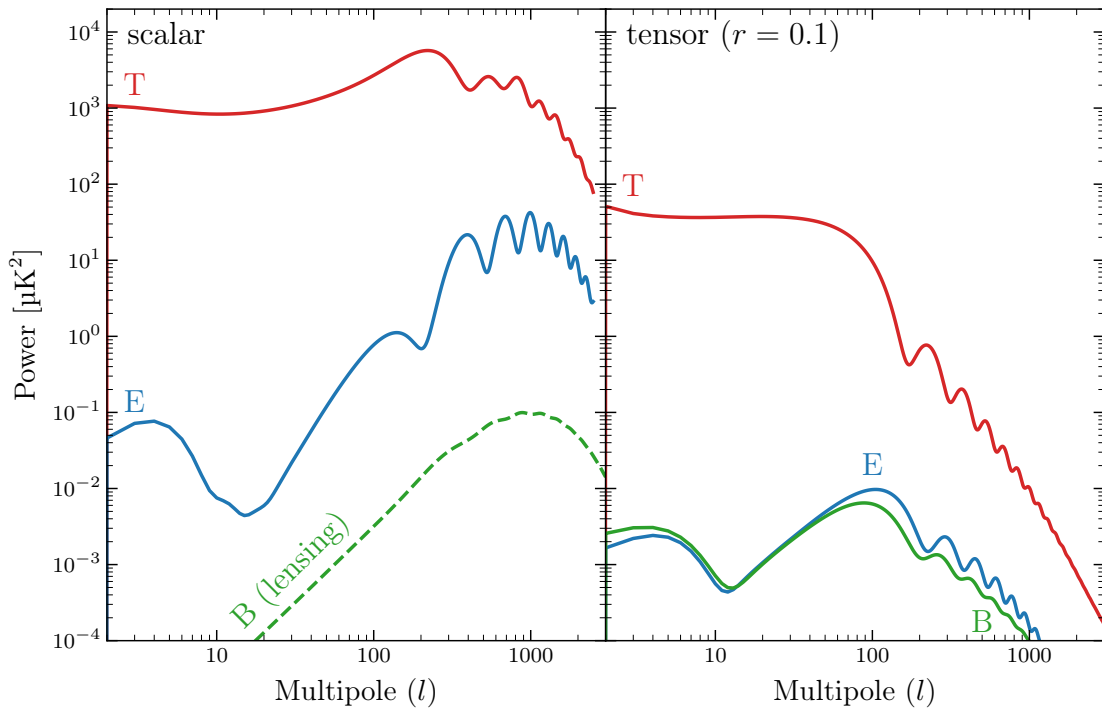


Fig. 7.37 | Summary of the CMB spectra arising from primordial scalar perturbations (*left*) and tensor perturbations (*right*). To avoid clutter, we didn't plot the TE cross spectra.

From Primordial to CMB Spectrum

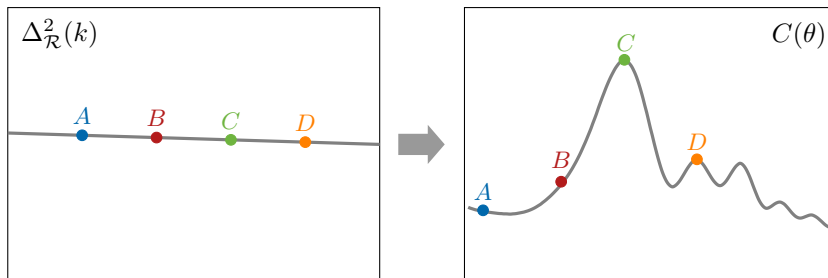


Fig. 8.6 The primordial spectrum of curvature perturbations (*left*) excite sound waves in the photon–baryon plasma, leading to oscillatory features in the spectrum of CMB anisotropies (*right*). Since this evolution is well understood, observations of the CMB can be used to constrain the primordial spectrum.

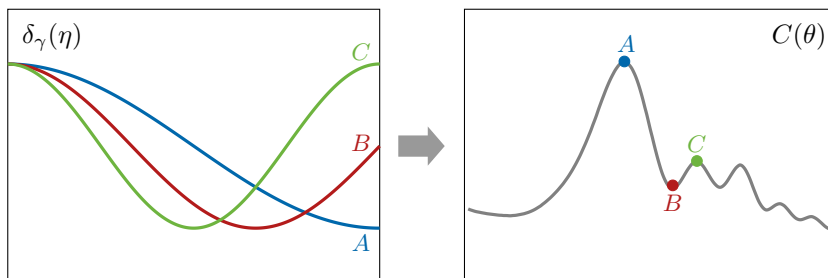


Fig. 8.7 Cartoon illustrating how sound waves in the primordial plasma (*left*) are associated to the peak structure of the CMB power spectrum (*right*). If all waves start with the same initial phase, then their amplitudes at photon decoupling will depend on their wavelengths (or oscillation frequencies). Waves that are captured at an extremum (*A* or *C*) produce the peaks in the CMB spectrum, while waves that have zero amplitude at decoupling (*B*) produce the troughs.

Constraints on the Tensor Amplitude

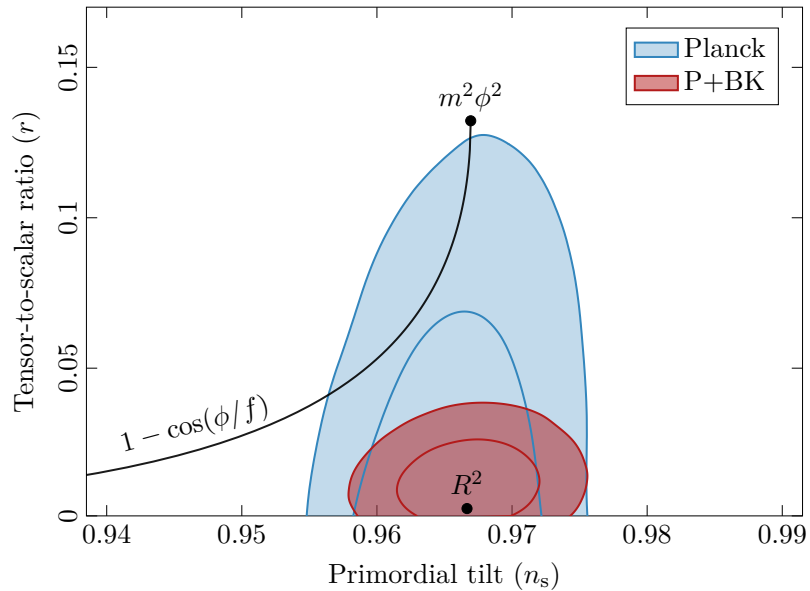


Fig. 8.9 Current constraints on the spectral tilt n_s and the tensor-to-scalar ratio r from CMB measurements of Planck and BICEP [14]. Shown are also the predictions of a few popular slow-roll models.

Local Non-Gaussianity

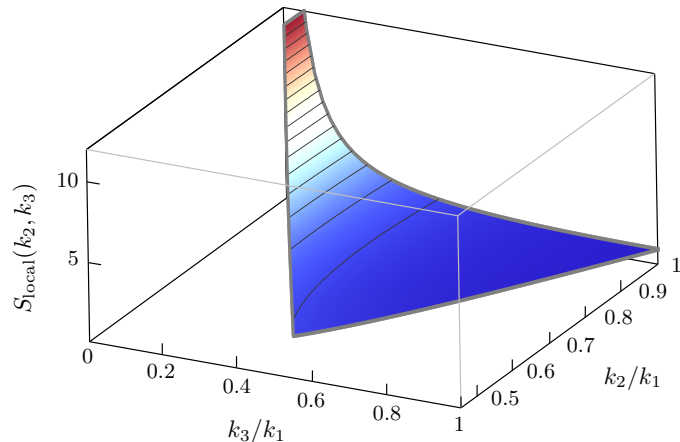


Fig. 8.10 Bispectrum of local non-Gaussianity. The signal is peaked for squeezed triangles with $k_3/k_1 \rightarrow 0$.

Equilateral Non-Gaussianity

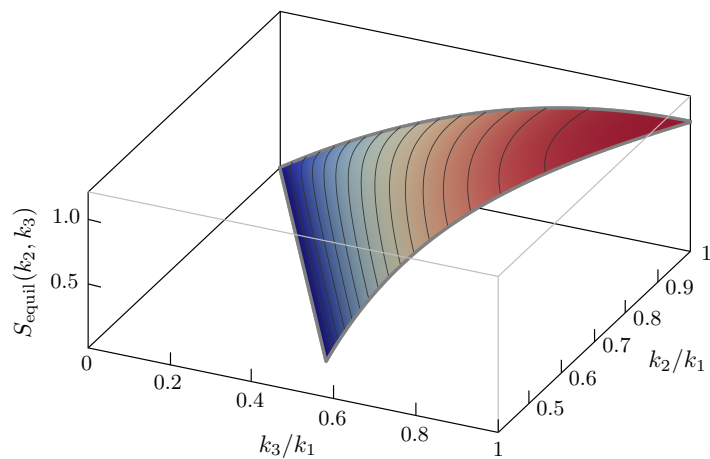


Fig. 8.11 Bispectrum for equilateral non-Gaussianity as described by the template shape (8.145). The signal is peaked for equilateral triangles with $k_3/k_1 \approx k_2/k_1 \approx 1$.

Folded Non-Gaussianity

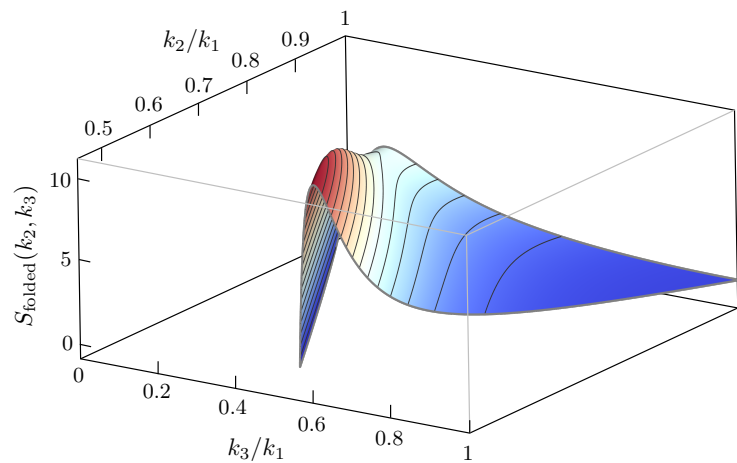


Fig. 8.12 Bispectrum for folded non-Gaussianity as described by the template shape (8.148), for $k_c/k_1 = 0.1$. The signal is peaked for folded triangles with $k_2 + k_3 \approx k_1$.

References

- [1] E. Hubble, “A Relation Between Distance and Radial Velocity Among Extra-Galactic Nebulae,” *Proceedings of the National Academy of Sciences* **15** no. 3, (1929) 168–173.
- [2] E. Hubble and M. Humason, “The Velocity-Distance Relation Among Extra-Galactic Nebulae,” *Astrophys. J.* **74** (1931) 43–80.
- [3] E. Corbelli and P. Salucci, “The Extended Rotation Curve and the Dark Matter Halo of M33,” *Mon. Not. Roy. Astron. Soc.* **311** no. 2, (2000) 441–447.
- [4] N. Aghanim *et al.* [Planck Collaboration], “Planck 2018 Results. VI. Cosmological Parameters,” *Astron. Astrophys.* **641** (2020) A6.
- [5] D. Scolnic *et al.*, “The Complete Light-Curve Sample of Spectroscopically Confirmed SNe Ia from Pan-STARRS1 and Cosmological Constraints from the Combined Pantheon Sample,” *Astrophys. J.* **859** no. 2, (2018) 101.
- [6] D. Fixsen *et al.* [COBE Collaboration], “The Cosmic Microwave Background Spectrum from the Full COBE FIRAS Data Set,” *Astrophys. J.* **473** (1996) 576, [arXiv:astro-ph/9605054](https://arxiv.org/abs/astro-ph/9605054).
- [7] C. Pitrou, A. Coc, J.-P. Uzan, and E. Vangioni, “Precision Big Bang Nucleosynthesis with Improved Helium-4 Predictions,” *Phys. Rept.* **754** (2018) 1–66.
- [8] S. Chabanier, M. Millea, and N. Palanque-Delabrouille, “Matter Power Spectrum: from Ly α Forest to CMB Scales,” *Mon. Not. Roy. Astron. Soc.* **489** no. 2, (2019) 2247–2253.
- [9] F. Beutler *et al.* [BOSS Collaboration], “The Clustering of Galaxies in the Completed SDSS-III Baryon Oscillation Spectroscopic Survey: Baryon Acoustic Oscillations in the Fourier Space,” *Mon. Not. Roy. Astron. Soc.* **464** no. 3, (2017) 3409–3430.
- [10] N. Aghanim *et al.* [Planck Collaboration], “Planck 2018 Results. I. Overview and the Cosmological Legacy of Planck,” *Astron. Astrophys.* **641** (2020) A1.
- [11] K. Story *et al.* [SPT Collaboration], “A Measurement of the Cosmic Microwave Background Damping Tail from the 2500-square-degree SPT-SZ Survey,” *Astrophys. J.* **779** (2013) 86.
- [12] J. Lesgourgues, *The Cosmic Linear Anisotropy Solving System (CLASS) I: Overview*, 2011. [arXiv:1104.2932](https://arxiv.org/abs/1104.2932) [astro-ph.IM].
- [13] S. Dodelson and F. Schmidt, *Modern Cosmology*. Academic Press, 2020.
- [14] P. Ade *et al.* [BICEP/Keck Collaboration], “BICEP/Keck XIII: Improved Constraints on Primordial Gravitational Waves using Planck, WMAP, and

BICEP/Keck Observations through the 2018 Observing Season,”
[arXiv:2110.00483 \[astro-ph.CO\]](https://arxiv.org/abs/2110.00483).